Journal of Iberian Geology
https://doi.org/10.1007/s41513-025-00327-4

RESEARCH PAPER

Emplacement kinematics of Cisuralian subvolcanic intrusions in the Iberian Chain (NE Spain): new insights from the structural and magnetic study of the Cerro Redondo dacitic intrusion

U. Majarena[1] · O. Pueyo[1] · A. Gil-Imaz[1] · C. Galé[1] · M. Lago[1] · B. Bauluz[1] · A. Rodríguez-Pintó[2]

Received: 20 October 2024 / Accepted: 31 October 2025

Abstract
A combined structural, petrological, and anisotropy of magnetic susceptibility (AMS) study of the Cisuralian (285 ± 2 Ma) Cerro Redondo dacitic intrusion (Iberian Chain, NE Spain) has been conducted to reconstruct its emplacement kinematics and determine its 3D geometry at the outcrop scale. This small igneous body, covering only 0.17 km^2, displays a well-defined magmatic foliation that is affected by asymmetrical, steeply plunging folds at different scales. Our multidisciplinary analysis suggests that the Cerro Redondo intrusion formed through the emplacement of successive magma pulses, during which the original magmatic foliations were passively folded. Detailed AMS data reveal a superposition of three kinematic processes recorded in the magnetic fabric, all occurring prior to complete crystallization: the development of an early planar magmatic fabric, localized simple shear deformation, and subsequent folding of the magmatic foliation. This integrated structural, petrological, and AMS study indicates that the Cerro Redondo intrusion is a sub-vertical, asymmetric subvolcanic body, emplaced at upper crustal levels under the control of extensional (or transtensional) movements of the late-Variscan Pardos Fault.

Keywords Magmatic folds · Magnetic fabric · Subsolidus · Cisuralian calc-alkaline magmatism · Iberian Chain

Resumen
Se ha llevado a cabo un estudio estructural, petrológico y de anisotropía de la susceptibilidad magnética (ASM) de la intrusión dacítica cisuraliense de Cerro Redondo (Cordillera Ibérica, NE de España) para reconstruir su cinemática de emplazamiento antes de la completa cristalización del magma y determinar su geometría tridimensional. Este cuerpo ígneo, con una extensión en planta de tan solo 0,17 km^2, presenta una foliación magmática bien definida afectada a diferentes escalas por pliegues asimétricos de pronunciada inclinación. Este estudio multidisciplinar nos ha permitido interpretar que la intrusión de Cerro Redondo se formó por el emplazamiento de sucesivos pulsos magmáticos que fueron plegando pasivamente las foliaciones ígneas originales. El análisis detallado de la ASM de la intrusión indica una superposición de tres procesos cinemáticos que ocurrieron antes de la completa cristalización del magma y que quedaron registrados en la fábrica magnética de las rocas: la formación de una fábrica magmática planar temprana, una deformación por cizalla simple en sectores localizados de la intrusión, y el plegamiento de la foliación magmática. Los datos estructurales, petrológicos y de ASM revelan que la intrusión de Cerro Redondo es un cuerpo subvolcánico asimétrico y subvertical, cuyo emplazamiento en los niveles superiores de la corteza estuvo controlado por el movimiento extensional (o transtensional) de la falla tardivarisca de Pardos.

Palabras Clave Pliegues ígneos · fábricas magnéticas · subsolidus · magmatismo cisuraliense calco-alcalino · Cordillera Ibérica

✉ A. Gil-Imaz
agil@unizar.es

U. Majarena
urbezmajarena@unizar.es

[1] Department of Earth Sciences - IUCA, University of Zaragoza, C/ Pedro Cerbuna nº12, 50009 Saragossa, Spain

[2] C.A.C.T.I, University of Vigo, C/ Fonte das Abelleiras, s/n, 36310 Pontevedra, Spain

Published online: 09 April 2026

1 Introduction

The anisotropy of magnetic susceptibility (AMS) is a powerful technique used to investigate the preferred orientation of magnetic minerals in rocks, providing valuable information on magmatic flow, tectonic deformation, and post-emplacement processes. Since pioneering works such as those by Balsley and Buddington (1960) and Stacey (1960), AMS has become a widely accepted method in structural geology and petrophysics. Subsequent studies, including that of Van der Voo and Klootwijk (1972), expanded the application of AMS to further unravel the petrofabric and emplacement mechanisms of granitic intrusions.

Over the last few decades, AMS has been extensively applied to granitic plutons and batholiths, particularly in orogenic contexts. Studies by Guillet et al. (1983), Bouchez et al. (1990), and Gleizes et al. (1993) pioneered the integration of AMS with petrographic and structural observations to infer magmatic flow directions and emplacement kinematics at the plutonic scale. These works established some of the methodological bases for interpreting magnetic fabrics as indicators of magma kinematic and syn-emplacement deformation.

In the Iberian Massif, AMS studies have played a central role in reconstructing the emplacement of granitic bodies during the late stages of the Variscan orogeny. Research conducted in NW Iberia, such as that of Román-Berdiel et al. (1995) and Aranguren et al. (1996), revealed how magnetic fabrics reflect the interplay between magmatic processes and regional tectonics. More recently, comprehensive reviews and regional-scale studies have been presented for the Variscan granites of NW Iberia (Sant'Ovaia et al., 2024) and the Pyrenean domain (Porquet et al., 2017), emphasizing the diversity of AMS patterns and their structural implications.

In the Iberian Chain, Cisuralian calc-alkaline rocks have been the subject of several previous magnetic studies. Calvín et al., (2014, 2012) investigated the magnetic anomalies generated by these rocks, particularly near the locality of Loscos, where they modeled the main characteristics of the igneous bodies producing these anomalies. Gil et al. (2006) conducted an AMS study on fabrics related to igneous flow and thermal contraction in an andesitic sill. Subsequently, Gil et al. (2009) carried out further AMS studies to help decipher the kinematic emplacement model of an andesitic dyke in the late-Variscan Montalbán Massif sector. These cases highlight the potential of AMS to provide insights even in small, rapidly emplaced igneous bodies where structural overprints and rapid crystallization may complicate fabric interpretation.

This study presents an integrated analysis of geological mapping, petrological and petrostructural observations, and detailed anisotropy of magnetic susceptibility (AMS) data from the Cerro Redondo dacitic intrusion. The objective is to unravel the complex sequence of petro-structural processes, including magma injection, strain-related shearing, and folding, that occurred prior to the complete magma crystallization. A petro-structural model consistent with the late-Variscan tectonic framework is proposed.

2 Geological setting

Cisuralian magmatism in the Iberian Chain, located in the northeast area of the Iberian Peninsula (Fig. 1a), is characterized by calc-alkaline affinity and comprises hundreds of metric- to hectometric- scale outcrops with a regional distribution associated with strike-slip normal faults in both the Aragonian and Castilian Branches (Lago et al., 2004) (Fig. 1b). The magmatic rocks range in composition from rhyolites to basaltic andesites and were primarily emplaced as subvolcanic dykes and sills. Some volcanic deposits, such as block-and-ash pyroclastic flows, have also been identified. The only known plutonic body related to this activity is the Loscos gabbro (Lago et al., 2004, 2005). Radiometric data indicate that this magmatism occurred between 294 and 285 Ma (Majarena et al., 2023a and references therein).

In the southwest sector of the Badules Unit (Carls, 1983) the magmatism is represented by subvolcanic felsic intrusions, mainly exposed in the areas of Castejón de las Armas and Pardos (Lago et al., 1992) (Fig. 1). These intrusions are aligned along late-Variscan strike-slip faults, ranging between NW–SE and NE–SW in the Castejón de las Armas area, and between NW–SE and E–W in the Sierra de Pardos area (Fig. 2a).

At a regional scale, the main structure of the Sierra de Pardos area is a NW–SE trending thrust fault and its associated hanging-wall anticline (the Sierra de Pardos Anticline), which involves Cambrian and Ordovician rocks overlying Triassic deposits (Fig. 2b). This fault is associated with the emplacement of five rhyolitic bodies during Late-Variscan times and was reactivated during the Alpine Orogeny (Majarena et al., 2017a).

The Cerro Redondo intrusion is situated in the southwestern normal limb of the Sierra de Pardos Anticline and represents the only dacitic intrusion in the Badules Unit (Fig. 2a). This igneous body has an age of 285 ± 2 Ma (Majarena et al., 2017a) and is hosted in the Borrachón Formation (Wolf, 1980), represented by Lower Ordovician black shales and quartzites that are mainly NW–SE oriented.

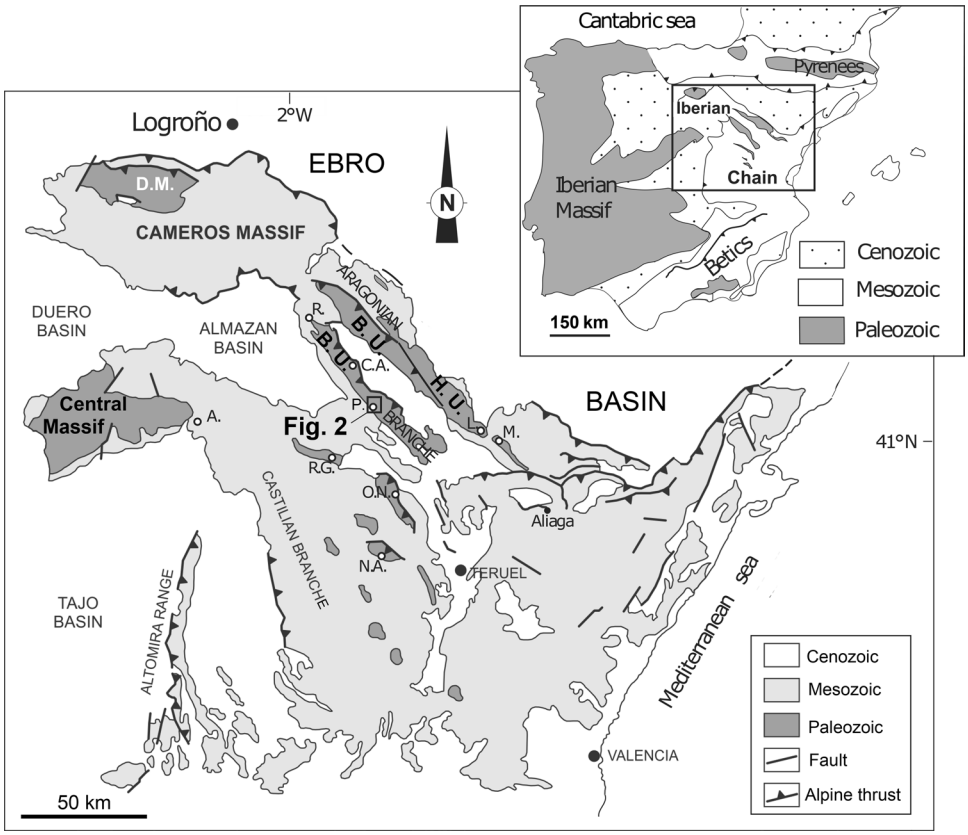

Fig. 1 Location of the studied area and geological setting within the central sector of the Iberian Chain (D.M.: Demanda Massif, B.U.: Badules Unit, H.U.: Herrera Unit). The location of Permian igneous outcrops is also shown: A.: Atienza, C.A.: Castejón de las Armas, L.: Loscos, M.; Maicas, N.A.: Noguera de Albarracín, O.N.: Ojos Negros, P.: Pardos, R.: Reznos, R.G.: Río de Gallo

3 The Cerro Redondo intrusion: geometry and structure

The Cerro Redondo intrusion is a small-scale, Artinskian (Cisuralian), calc-alkaline dacitic subvolcanic body located in the Iberian Chain (NE Spain). It offers excellent outcrop conditions, distinctive petrological features, and a well-developed magmatic foliation defined by regular planar structures clearly visible in the field, allowing the recognition of early emplacement stages. These characteristics have enabled us to unravel the strain evolution associated with flow dynamics during the initial phases of emplacement. The relative homogeneity in both composition and texture, the presence of folded magmatic foliation at various scales, serving as strain markers, and the limited size of the intrusion, provide highly favorable conditions for reconstructing flow and strain processes linked to rapid changes in pressure and temperature conditions.

At a cartographic scale, the body displays an elliptical shape with an outcrop area of 0.17 km^2, elongated in a NW–SE direction, subparallel to the structural orientation of the host rocks. The intrusion is affected by two main subparallel faults trending E–W to NE–SW: the late-Variscan Pardos fault, which defines the northern boundary of the igneous body, and the Cerro Redondo fault, which postdates the intrusion (Fig. 3).

The host rocks consist of black shales interbedded with quartzites belonging to the Borrachón Formation (Lower Ordovician), with an orientation ranging from N116E to N156E and dips between 40° and 80° to the southwest (mean value of N139,54° SW; Fig. 3). The general orientation of the intrusion is roughly parallel to the fabric of the host rocks, although the igneous body crosscuts this fabric at both the NW and SE margins. In this sector of the Iberian Chain, Mesozoic rocks (Lower Triassic unit) unconformably overlie the Palaeozoic rocks, displaying NW-SW strikes and mean dips of approximately 30° to the southwest.

4 Methodology

4.1 Structural mapping and petrological samples

The orientation and dip of the magmatic foliation were measured at 166 sites to determine its geometric pattern throughout the entire intrusion. Additionally, the orientation and dip of bedding planes in the host rocks were recorded at 22 points surrounding the intrusion. A detailed structural analysis was performed on 19 magmatic folds, ranging from decimetric to metric scale, including measurements of orientation and dip of the magmatic foliation affected by

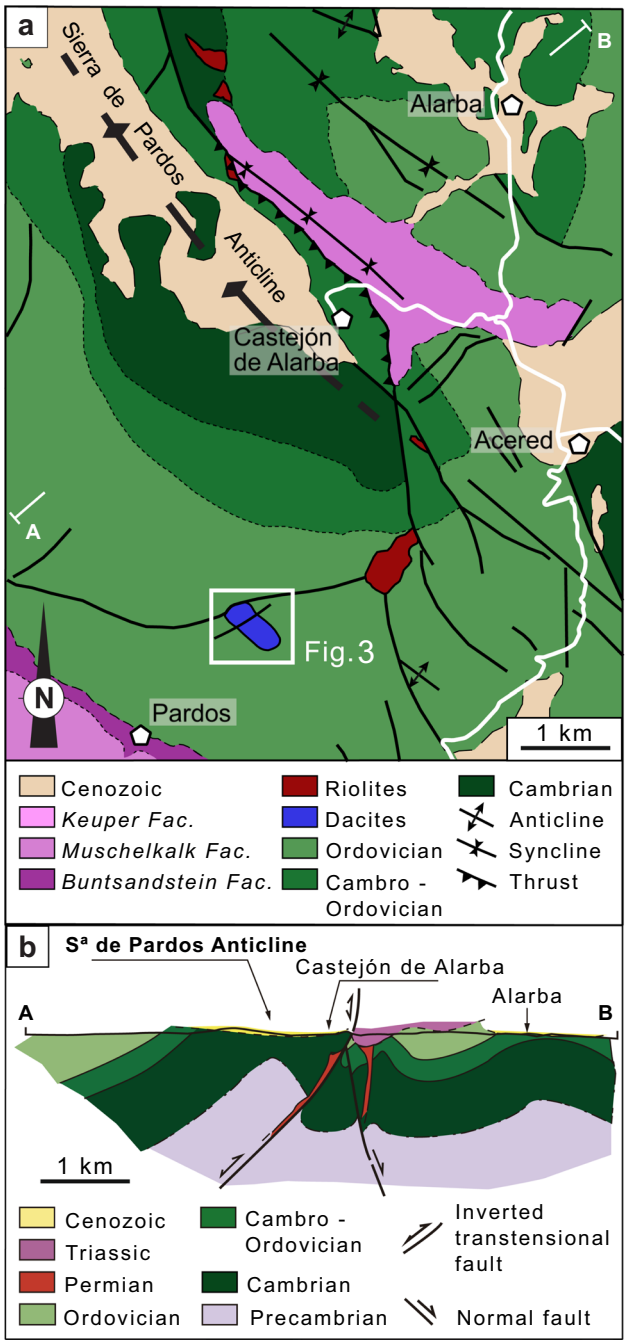

Fig. 2 **a** Geological map of the Sierra de Pardos area. **b** Geological cross-section of the Sierra de Pardos Anticline (see trace in map 2a)

folding. Furthermore, 25 sampling sites were selected for both petrological and AMS analyses.

The petrographic study was conducted on polished sections of 100 samples collected from the intrusion, with four representative samples taken from each site. After scanning the sections, a systematic grid of 196 analysis points per section was defined for petrographic characterization, identifying the groundmass or phenocryst type at each point. In addition, thin sections from 17 sample sites were also analyzed. Bulk density was determined on the same 100 samples (4 per site), using laboratory weight measurements and calculated volumes (all ASM specimens were cylinders measuring 2.08 cm in height and 2.54 cm in diameter, yielding a volume of 10.55 cm^3).

4.2 AMS methodology

Samples for the magnetic fabric analysis were collected from 25 individual sites (Fig. 3). Seven of them (CR-01 to CR07) were drilled across asymmetric meter-scale folds distributed along the entire extent of the intrusion. At each site, 3 to 23 oriented cores were extracted, measuring 6 to 15 cm in length and 2.54 cm diameter, using a portable gasoline-powered drill. From each core, 1 to 5 cylindrical specimens with a height-to-diameter ratio of 0.82 were prepared.

Anisotropy of magnetic susceptibility (AMS) was measured on a total of 490 specimens using a KLY3-S Kappabridge (AGICO) susceptometer, operating at 875 Hz and 300 A/m, in the Magnetic Fabrics Laboratory of the Geotransfer Research Group of the Earth Sciences Department, University of Zaragoza (Spain).

Data analysis included the orientation of the main susceptibility axes (Kmax, Kint and Kmin) in stereographic projection, the mean susceptibility axes module, and the anisotropy of magnetic susceptibility ellipsoid, using different parameters: magnetic foliation (F), magnetic lineation (L), the shape parameter (T), and the degree of corrected anisotropy (P') (see Jelinek, 1981; Hrouda, 1982 and Tarling & Hrouda, 1993, for definitions of magnetic parameters). The statistical distribution of the susceptibility axes was evaluated following Jelinek (1977), using ANISOFT 4.2 software (Chadima & Jelinek, 2008).

Magnetic susceptibility variations with temperature were analyzed in 8 samples using a CS-3 furnace plugged into the AGICO KLY3-S equipment, under an argon atmosphere. Susceptibility changes were recorded in heating and cooling curves, ranging from room temperature up to 700 °C (Hrouda, 1994; Jordanova & Jordanova, 2016). Curve processing, Curie temperatures and paramagnetic contributions were determined using Cureval 8 software (Chadima & Hrouda, 2009). These measurements were also conducted at the Magnetic Fabrics Laboratory of the Earth Sciences Department, University of Zaragoza (Spain).

Additionally, magnetic susceptibility changes and saturation were also studied through DC susceptibility measurements under increasing and subsequently decreasing fields ranging from − 0.5 to 0.5 T, at room temperature. Coercivity of ferromagnetic phases was assessed by measurings hysteresis loops on representative micro samples (ranging from 20 to 26 mg) using a PPMS (Quantum Design) at the CACTI Technological Center of the University of Vigo (Spain).

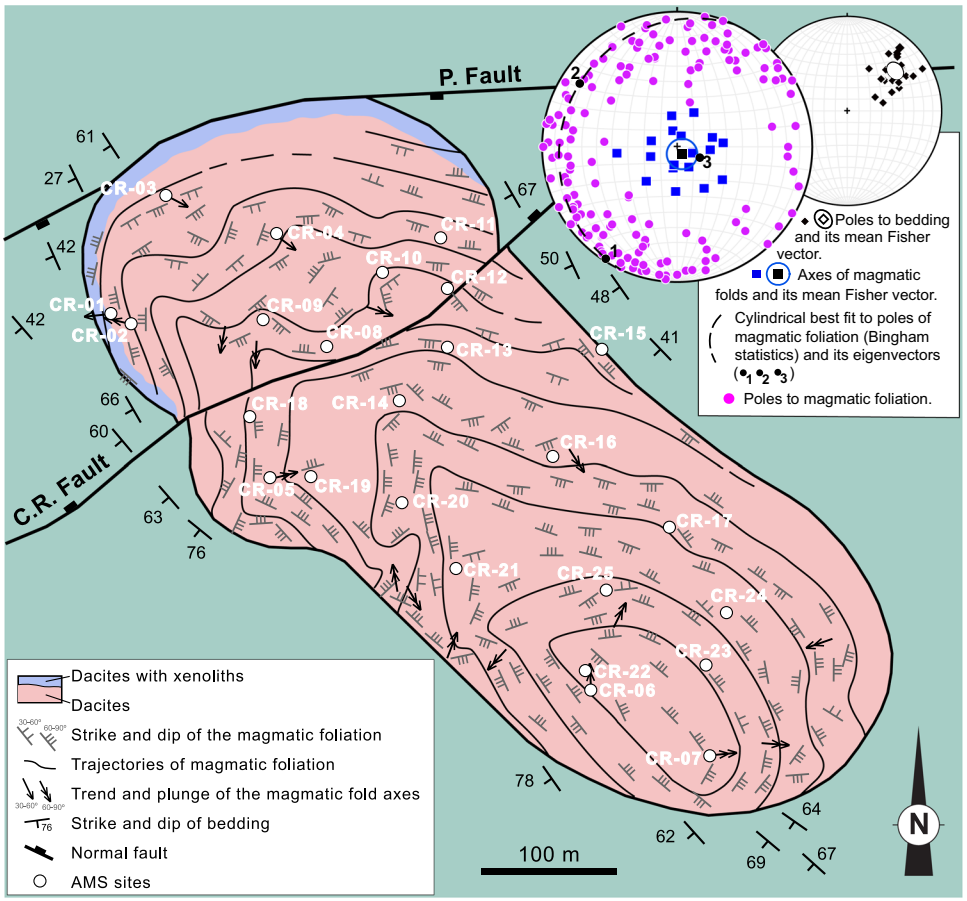

Fig. 3 Structural map of the Cerro Redondo intrusion and stereoplots showing magmatic fold axes, poles to magnetic foliation and bedding of the host-rock

5 Results

5.1 Petrology and petrography

From a petrological and petrographic perspective, the igneous rocks of the Cerro Redondo intrusion are porphyritic dacites containing 10–40% phenocrysts. These phenocrysts consist of quartz (7–20%), sanidine (6–22%) and biotite (0–5%) (Fig. 4a), with individual crystal sizes ranging from 0.5 to 3 mm (Fig. 4b). They are embedded in a microcrystalline or glassy matrix composed of sanidine, quartz and accessory minerals such as apatite, monazite and zircon (Fig. 4b, c). Samples collected from folded sites frequently exhibit kinked and bent biotite crystals (Fig. 4d–f), which clearly indicates solid-state deformation (Bouchez et al., 1992; Paterson et al., 1989, 1998; Buttner, 1999; Pawley & Collins, 2002; Passchier & Trouw, 2005; Fazio et al., 2020).

Regarding phenocrysts distribution within the intrusion, a progressive decrease in sanidine content is observed toward the northwest (Fig. 5a), while biotite content (the main Fe-rich paramagnetic phase in the studied samples) appears to increase in that direction (Fig. 5b). Quartz phenocrysts content does not display any clear spatial trend. Additionally, both sample density and magnetic susceptibility values show a marked increase towards the northern and northwestern margins of the intrusion (Fig. 5c, d).

The intrusion contains xenoliths of black shales and some quartzites comparable to the surrounding host rocks. These xenoliths range in size from 1 mm to 15 cm (Fig. 6a) and tend to cluster near the northwestern contact, especially along the northern sector adjacent to the Pardos fault.

5.2 Structural and cartographic data

The main structural feature of the intrusion is a well-defined magmatic foliation with steep dips and a relatively consistent spacing that varies with the scale of observation (Fig. 6b). Foliation spacing ranges from 1 to 30 cm across the intrusion, tending to be more closely spaced near the margins and more widely spaced toward the center. However, this distribution is irregular and does not follow a systematic pattern throughout the body. Foliation dip angles range between 50° and 90°, with the steepest dips concentrated in the southeastern sector, where a clear concentric pattern is observed, and shallower dips toward the northwestern margin (Fig. 3). A widespread structural feature is the presence of metric-scale folds affecting the magmatic foliation throughout the intrusion (Fig. 6c–e).

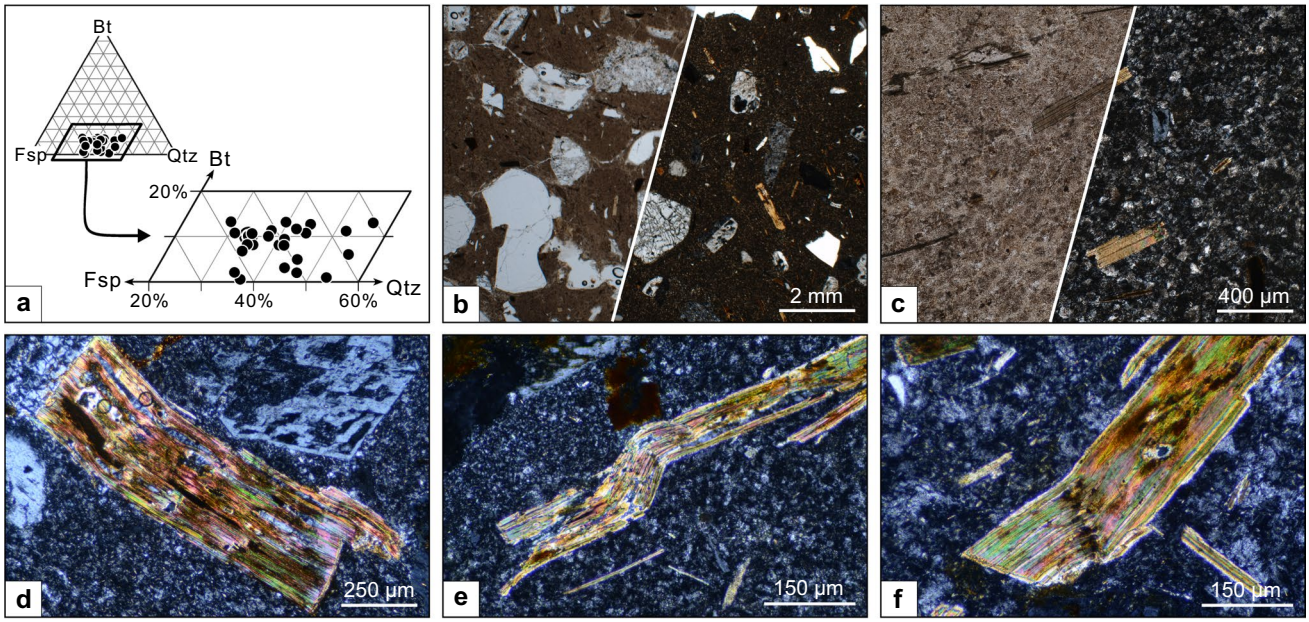

Fig. 4 Petrographic composition and microphotographs. **a** Variation in the volume percentage of biotite, feldspar and quartz phenocrysts in the analyzed samples. **b, c** Microphotographs under plane-polarized (left) and cross-polarized light (right), showing general texture (**b**) and matrix detail (**c**). **d, e, f** Microphotographs under cross-polarized light showing examples of bent and kinked magmatic biotite crystals

At the scale of the entire intrusion, traces of the magmatic foliation roughly outline a sub-vertical hectometre-scale fold with a mean axial trace trending NW–SE (Fig. 3). Within the body, decametre- to metre-scale folds are predominant in the northwestern sector, whereas minor folds ranging from metre- to decimetre-scale, with a main orientation parallel to the local intrusion contacts, are more common in the southeastern sector.

At the outcrop scale, the magmatic folds are typically irregular and asymmetrical, displaying Type 2 and 3 geometries (Ramsay, 1967), and locally defining Type threefold interference patterns (Fig. 6d) (Ramsay, 1967). Fold axes exhibit variable orientations with steep plunges ranging from 55° to 83° (Fig. 3). Similar to the pattern observed in foliation dips, the steepest axial plunges are found in the southeastern sector, while the shallowest occur near the northwestern boundary (Fig. 3).

Additionally, the poles to the magmatic foliation planes show a wide dispersion. However, they collectively define a mean NNE-SSW oriented movement plane at the intrusion scale, whose pole (Fig. 3) closely coincides with the average trend of the main fold axis identified throughout the igneous body.

Regarding the host rocks, although the general trend of bedding/cleavage surfaces is roughly parallel to the magmatic foliation, clear cross-cutting relationships are observed in the northwestern and southeastern contacts of the intrusion (Fig. 3).

5.3 Magnetic study

5.3.1 Magnetic susceptibility and magnetic carries

The mean susceptibility (Km) values per site show a wide range, from 35 to 191×10^{-6} SI (Table 1). As shown on the map (Fig. 5d), the spatial distribution of Km closely mirrors the biotite distribution pattern, with the highest Km values found in the northwestern sector of the intrusion and the lowest values in the southeastern sector. The corrected degree of anisotropy (P') has a mean value of 1.021 and shows no clear correlation with Km, except at three sites in the northwesternmost part of the intrusion (CR-01, CR-03, CR-04), where the highest Km values suggest a notable ferromagnetic contribution (Fig. 7a).

Henkel's plot (1976) of density versus magnetic susceptibility data (Fig. 7b) shows a noisy relationship between both variables, with a low correlation coefficient (R = 0.33). This low correlation coefficient between density and magnetic susceptibility is very similar to that reported by Pueyo et al., (2022) in the Pyrenees for the granodiorites of the variscan Maladeta pluton (R = 0.34), and may be related to the later alteration processes that affected the intrusion.

The mean Km values remain below 200×10^{-6} SI units, indicating a predominantly paramagnetic origin (Pueyo-Anchuela et al., 2013; Rochette, 1987). Therefore, except for those few sites where ferromagnetic influence may be significant, the observed susceptibility can be linked to

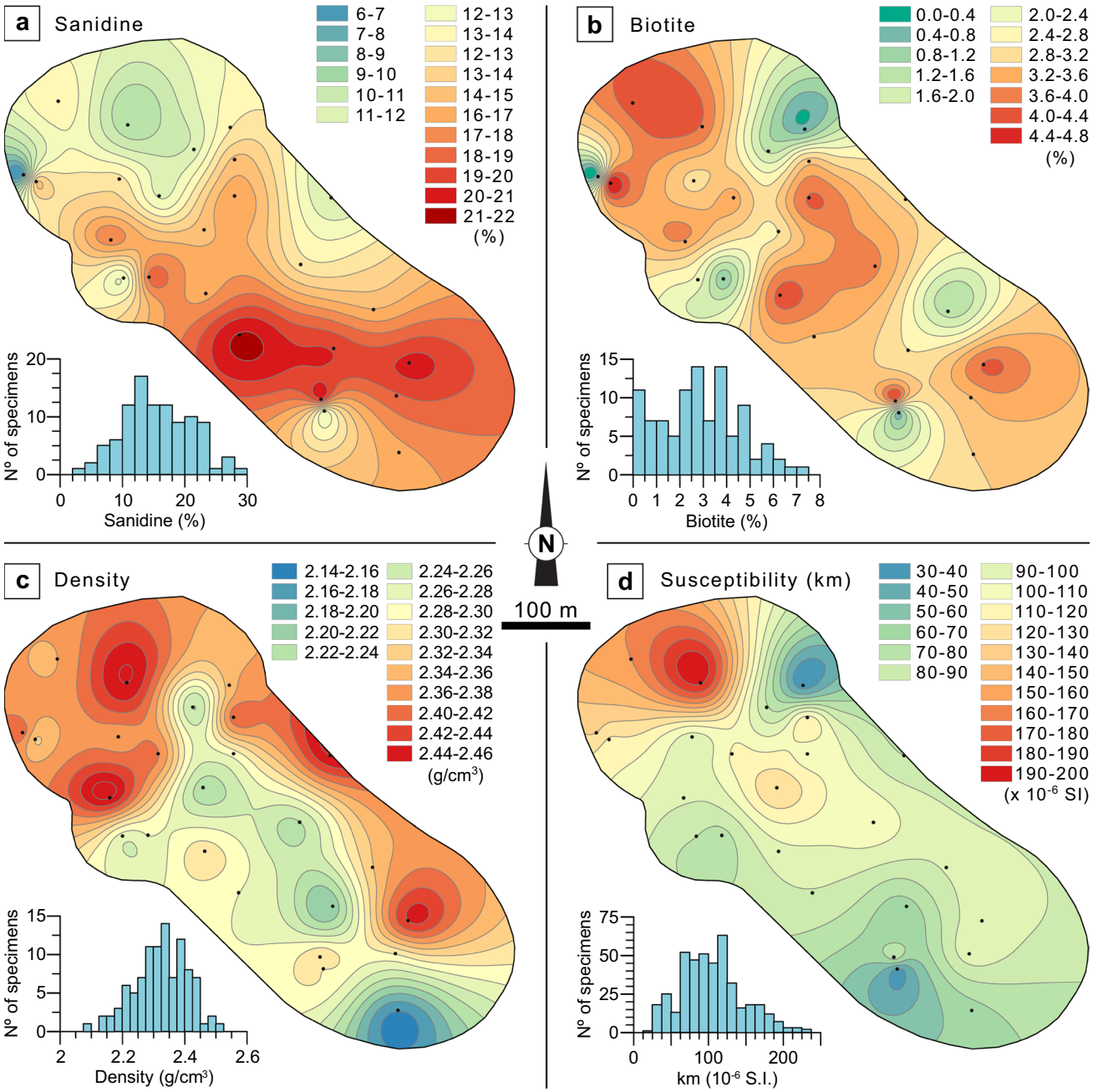

Fig. 5 Spatial variation maps and histograms of the percentage of sanidine (**a**) and biotite phenocrysts (**b**), sample density (**c**) and site-mean susceptibility (Km) values (**d**) for the Cerro Redondo intrusion

iron-bearing paramagnetic silicates such as biotite (Bouchez, 1997; Gleizes et al., 1993).

Thermomagnetic susceptibility curves (K-T curves) display a marked decrease in susceptibility with increasing temperature between 25 and 140 °C (Fig. 8a). The paramagnetic hyperbolic fitting shows contributions ranging from 56 to 98.4%. As shown in Fig. 8a, the magnetic susceptibility progressively decreases, with distinct susceptibility steps in the range of the Curie temperature of magnetite. Some samples even show a small Hopkinson effect (e.g. CR07-05 in Fig. 8a). A sharp drop in susceptibility is observed near the Néel temperature (hematite temperature). These features are characteristic of samples containing both magnetite and hematite, but with overall susceptibility dominated by paramagnetic phases. One significant feature of the studied samples is the very rapid decrease in susceptibility at low temperatures, with steeper slopes than those predicted by the Curie–Weiss law. This behaviour suggests the presence of additional mineral phases reducing the susceptibility at temperatures below 100 °C, possibly related to hydrated

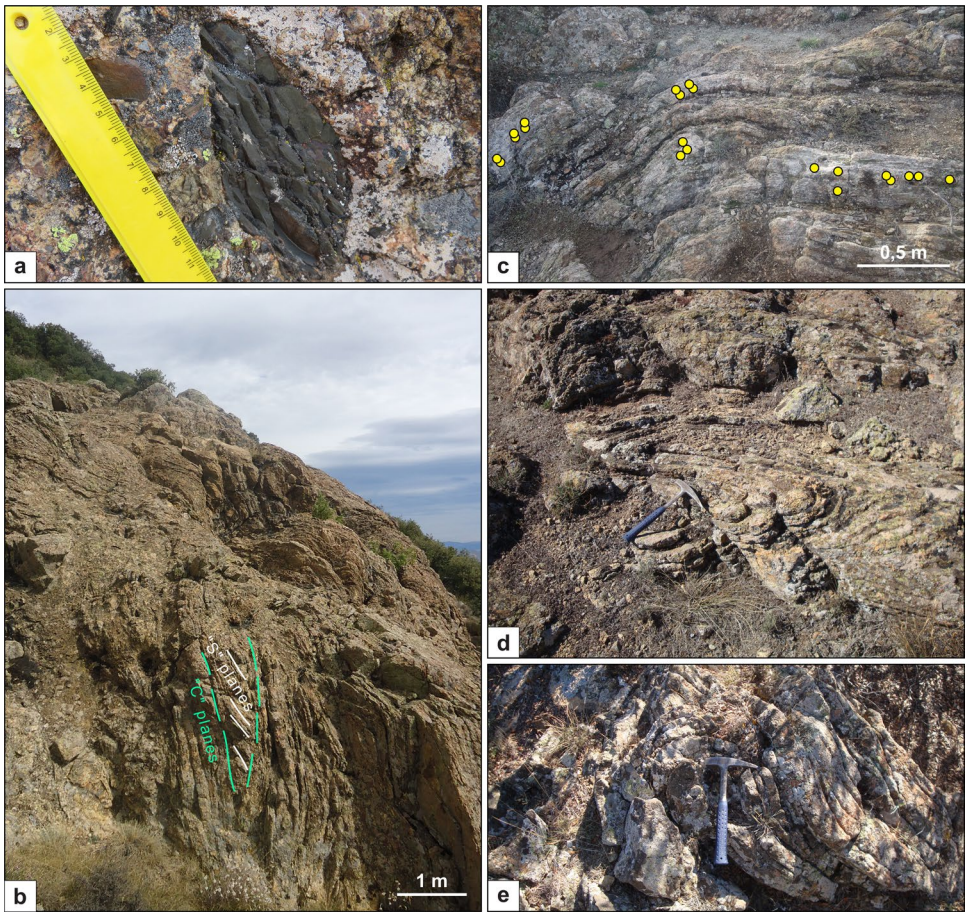

Fig. 6 Field aspects. **a** Centimeter-scale xenolith of black shale. **b** Subvertical well-developed magmatic foliation with regular and irregular spacing. Local "S-C" type structures are highlighted. **c** Sampling site (yellow dots mark sample locations) in a meter-scale magmatic fold (site CR-01, see location in Fig. 2). **d** Type 2 and threefold geometries (Ramsay, 1967), **e** Interference pattern of Type 3 folds (Ramsay, 1967),

ferromagnetic phases with non-stoichiometric composition, such as goethite, likely associated with weathering or alteration.

The susceptibility, independent of the applied field (e.g. paramagnetic and diamagnetic contribution), is high across all samples (Fig. 8b). Rapid saturation at low fields indicates the presence of mineralogical phases with low coercivity, which contribute to the susceptibility under the measurement conditions of the AMS. Hysteresis loops exhibit a wasp-waisted shape (Tauxe et al., 1996), supporting the presence of multiple ferromagnetic phases within the magnetite field, which can be interpreted in terms of changes in grain size. The main coercivity forces (H_c) range between 5 and 15 mT, typical of multidomain magnetites (e.g. Jackson et al., 1988).

5.3.2 Magnetic fabric

The overall AMS data across the intrusion reveal both planar and linear-planar fabrics, as indicated by the dispersion of the AMS axes and the confidence ellipses derived from Jelinek's statistics on stereographic projections (Fig. 9, data shown in Table 2).

As shown in Fig. 7c, the samples with the highest P' values also display the highest planarity, with a direct correlation between the P' and F parameters (Fig. 7c).

In general, the stereographic projections of the AMS directional data (Fig. 9, Table 2) show that the magnetic lineation lies within the magmatic foliation plane, and the magnetic foliation is either parallel or slightly oblique to the magmatic foliation plane (e.g. CR-09, CR-14, CR-15, CR-18, CR-22). In these cases, the magnetic foliation matches reasonably well with the anisotropy of the distribution of the axes within the Jelinek statistical ellipses (Fig. 9). In other cases, the distribution of the axes within the Jelinek´s statistical ellipses defines linear to linear-planar fabrics with the magnetic foliation plane perpendicular or oblique to the igneous foliation measured in the field (e.g., CR-11, CR-21). Additionally, in other sites with the same magnetic directional pattern as the previous ones but with well-defined linear-planar fabric (e.g. site CR-8, CR-10), the plane perpendicular to the magmatic foliation is defined by the Kmin and Kint axes.

Some sites located along metre-scale folds (CR-01 to CR-07) show a more scattered distribution of AMS axes. In all these cases, the magnetic lineation displays a high plunge, is contained within the magmatic foliation and

Table 1 Mean results from AMS and density analysis for the studied sites: coordinates, number of samples and mean values of mean susceptibility (km), lineation parameter (L), foliation parameter (F), corrected degree of anisotropy (P′) and shape parameter (T) and density (ρ)

Name	Position		n	Km (10^{-6} SI)		L		F		P′		T		ρ (kg/m^3)	
	X	Y		Mean	Desv	Mean	Desv	Mean	Desv	Mean	Desv	Mean	Desv	Mean	Desv
CR-01	613,137	4,556,654	47	129.8	14.3	1.004	0.002	1.008	0.005	1.012	0.006	0.263	0.34	2392	46
CR-02	613,152	4,556,646	49	119.0	11.0	1.006	0.003	1.025	0.006	1.033	0.007	0.585	0.19	2340	39
CR-03	613,178	4,556,741	43	160.1	16.3	1.010	0.004	1.008	0.004	1.018	0.004	- 0.159	0.35	2359	18
CR-04	613,260	4,556,713	26	191.2	20.0	1.011	0.003	1.013	0.006	1.024	0.004	0.043	0.36	2440	26
CR-05	613,255	4,556,532	31	80.4	15.2	1.007	0.002	1.007	0.003	1.014	0.004	0.034	0.33	2269	22
CR-06	613,492	4,556,375	34	37.3	5.6	1.005	0.003	1.008	0.004	1.014	0.004	0.219	0.45	2304	85
CR-07	613,580	4,556,326	40	65.7	5.7	1.004	0.002	1.005	0.003	1.009	0.003	0.114	0.43	2159	63
CR-08	613,297	4,556,629	8	111.3	10.0	1.013	0.004	1.022	0.007	1.036	0.006	0.217	0.26	2383	48
CR-09	613,250	4,556,649	9	95.8	8.3	1.001	0.001	1.026	0.006	1.031	0.007	0.892	0.04	2366	37
CR-10	613,338	4,556,684	11	81.1	4.4	1.007	0.004	1.011	0.002	1.019	0.004	0.255	0.22	2238	48
CR-11	613,381	4,556,710	10	35.4	4.6	1.005	0.002	1.007	0.003	1.012	0.003	0.177	0.35	2354	31
CR-12	613,386	4,556,672	10	112.4	5.8	1.016	0.003	1.013	0.004	1.029	0.004	- 0.104	0.23	2394	67
CR-13	613,386	4,556,629	9	105.0	6.2	1.003	0.001	1.014	0.002	1.018	0.002	0.695	0.13	2291	32
CR-14	613,350	4,556,589	9	127.1	6.9	1.007	0.002	1.019	0.003	1.027	0.002	0.488	0.17	2233	86
CR-15	613,500	4,556,627	11	79.6	7.3	1.004	0.003	1.027	0.005	1.034	0.004	0.726	0.21	2435	25
CR-16	613,464	4,556,548	12	106.0	3.6	1.010	0.002	1.007	0.003	1.018	0.002	- 0.171	0.27	2239	46
CR-17	613,550	4,556,495	9	91.2	5.2	1.009	0.001	1.011	0.002	1.020	0.002	0.061	0.11	2340	14
CR-18	613,240	4,556,577	11	91.5	10.2	1.005	0.004	1.028	0.003	1.036	0.004	0.691	0.21	2441	51
CR-19	613,285	4,556,533	13	77.0	7.0	1.004	0.002	1.006	0.002	1.010	0.002	0.148	0.32	2275	36
CR-20	613,352	4,556,514	17	95.6	8.8	1.007	0.002	1.010	0.006	1.017	0.006	0.079	0.29	2313	37
CR-21	613,392	4,556,465	11	89.4	4.4	1.004	0.003	1.009	0.004	1.014	0.003	0.305	0.53	2277	31
CR-22	613,488	4,556,389	18	73.0	6.8	1.006	0.003	1.010	0.002	1.016	0.003	0.302	0.30	2322	43
CR-23	613,577	4,556,393	17	94.8	9.4	1.008	0.005	1.010	0.004	1.018	0.004	0.139	0.41	2302	63
CR-24	613,592	4,556,432	16	94.2	3.3	1.005	0.001	1.015	0.003	1.020	0.004	0.516	0.12	2422	24
CR-25	613,503	4,556,449	18	65.7	7.3	1.005	0.002	1.018	0.010	1.025	0.013	0.581	0.20	2210	40
Mean				96.4		1.007		1.013		1.021		0.284		2324	
Desv				33.6		0.003		0.007		0.008		0.291		76	

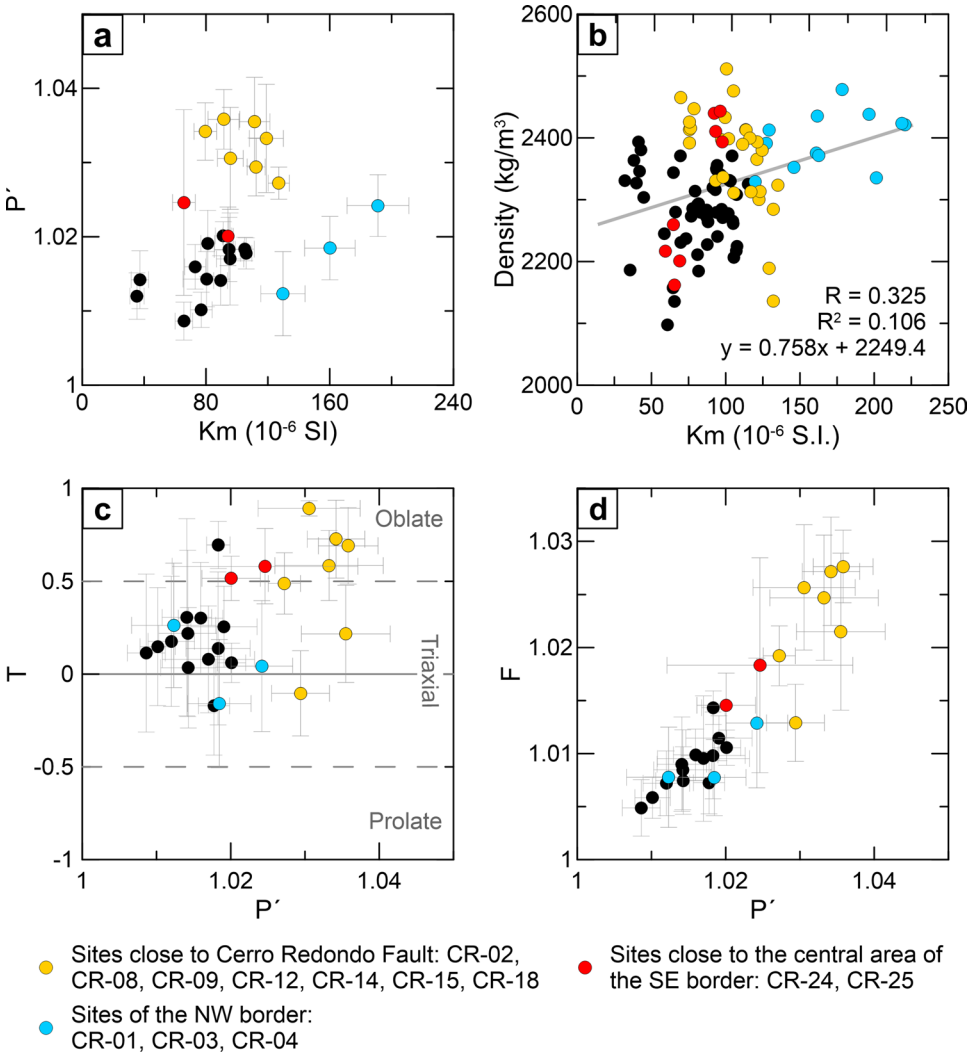

Fig. 7 AMS parameters (site mean and standard deviations, see Table 1 for values). **a** Mean magnetic susceptibility (Km) vs. corrected degree of anisotropy (P'). **b** Mean magnetic susceptibility (Km) vs. sample density. **c** Corrected degree of anisotropy (P') vs. shape parameter (T). **d** Corrected degree of anisotropy (P') vs. foliation parameter (F)

is close to the fold axis, affecting the magmatic foliation (Fig. 9, Table 2).

6 Discussion

Numerous studies have emphasized the need of detailed analysis to decipher the complexity of the intrusion and emplacement processes, especially when only the final product is accessible or when earlier stages of emplacement have been obliterated due to the internal homogenization of the igneous body (e.g. Jousselin et al., 2012). This challenge is often associated with the inherent heterogeneity of magmatic flow processes, where only the final stage of magma movement prior to complete crystallization tends to be preserved (Paterson et al., 1998).

The multidisciplinary approach adopted in the study of the Cerro Redondo intrusion enables the characterization of key geometrical features and provides valuable insights into the magmatic processes involved during its emplacement and subsequent growth.

6.1 The origin of a primary magmatic planar-rock fabric

Petro-structural processes responsible for the development of magmatic foliation can provide critical insights into intrusion growth, magma flow dynamics and the broader regional tectonic framework (e.g. Hutton, 1988; Megerssa et al., 2020; Paterson & Vernon, 1995; Paterson et al., 1998).

The absence of compositional or textural variations, such as cross-bedding or channel structures, within the studied intrusion suggests that the observed foliation is not related to compositional layering (Clarke & Clarke, 1998; Gawęda & Szopa, 2012; Jousselin et al., 2012; Namur et al., 2015; Pinotti et al., 2016).

On the other hand, the presence of small fragments of host rock concentrated along the northern margin of the intrusion, often oriented parallel or slightly oblique to both

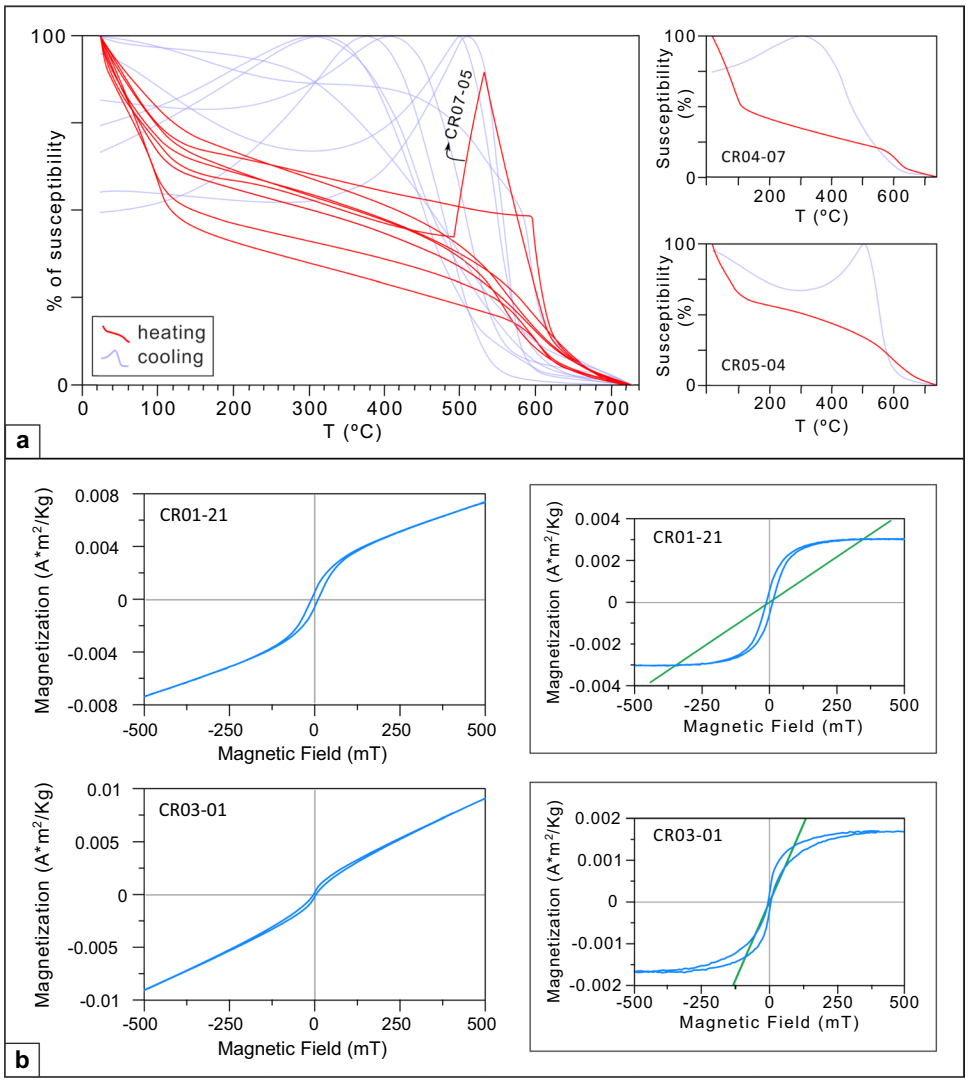

Fig. 8 Magnetic mineralogy characterization. **a** Susceptibility vs. temperature (K-T) curves for heating to 700 °C (red) and cooling back to 25 °C (blue) for eight representative samples. Detail for samples CR04-07 and CR05-04 is included. **b** Hysteresis loops for specimens CR01-21 and CR03-01, showing original and paramagnetic-subtracted curves (green lines in insets)

the intrusion boundary and pre-existing magmatic foliations, strongly supports the occurrence of shortening and/or shearing during emplacement against the host-rock interface. Additionally, the accumulations of strain resulting from successive magma pulses, exerting pressure against previously emplaced, high-viscosity magma sheets, may explain the development of new foliation surfaces. The generation of successive magmatic foliation surfaces can be attributed either to strain propagation from distal sectors relative to the host rocks during successive magma injections or to rheological changes in the magma under a constant regional strain regime, such as those induced by thermal variations (e.g. Paterson et al., 1998; Pons et al., 2006).

In summary, the planar fabric observed in the Cerro Redondo intrusion can be interpreted as steeply dipping magmatic surfaces generated by mechanical flattening against both host rock and pre-existing high-viscosity sheets (Paterson et al., 1989, 1998; Pinotti et al., 2006). The emplacement of earlier individualized magmatic layers (i.e.: magmatic foliations) would take place in the non-constricted central sector of the feeder zone (Fig. 10a). Two concurrent processes likely contributed to this fabric: (1) the development of a steeply plunging magnetic lineation aligned with the flow vector within the feeder zone, and (2) shear-induced deformation resulting from both relative movements between adjacent high-viscosity magma sheets and magma friction against the host-rock walls. This latter deformation mechanism accounts for the presence of imbricate magnetic fabrics and high-plunging folds near the feeder conduit (Fig. 10a). Given the high viscosity of the magma, such shear-induced deformation could have occurred at any stage throughout the emplacement process.

6.2 Timing of the magmatic folding

The development of folds in magmatic systems is classically attributed to passive folding mechanisms driven by magma injection and the transmission of magmatic pressure

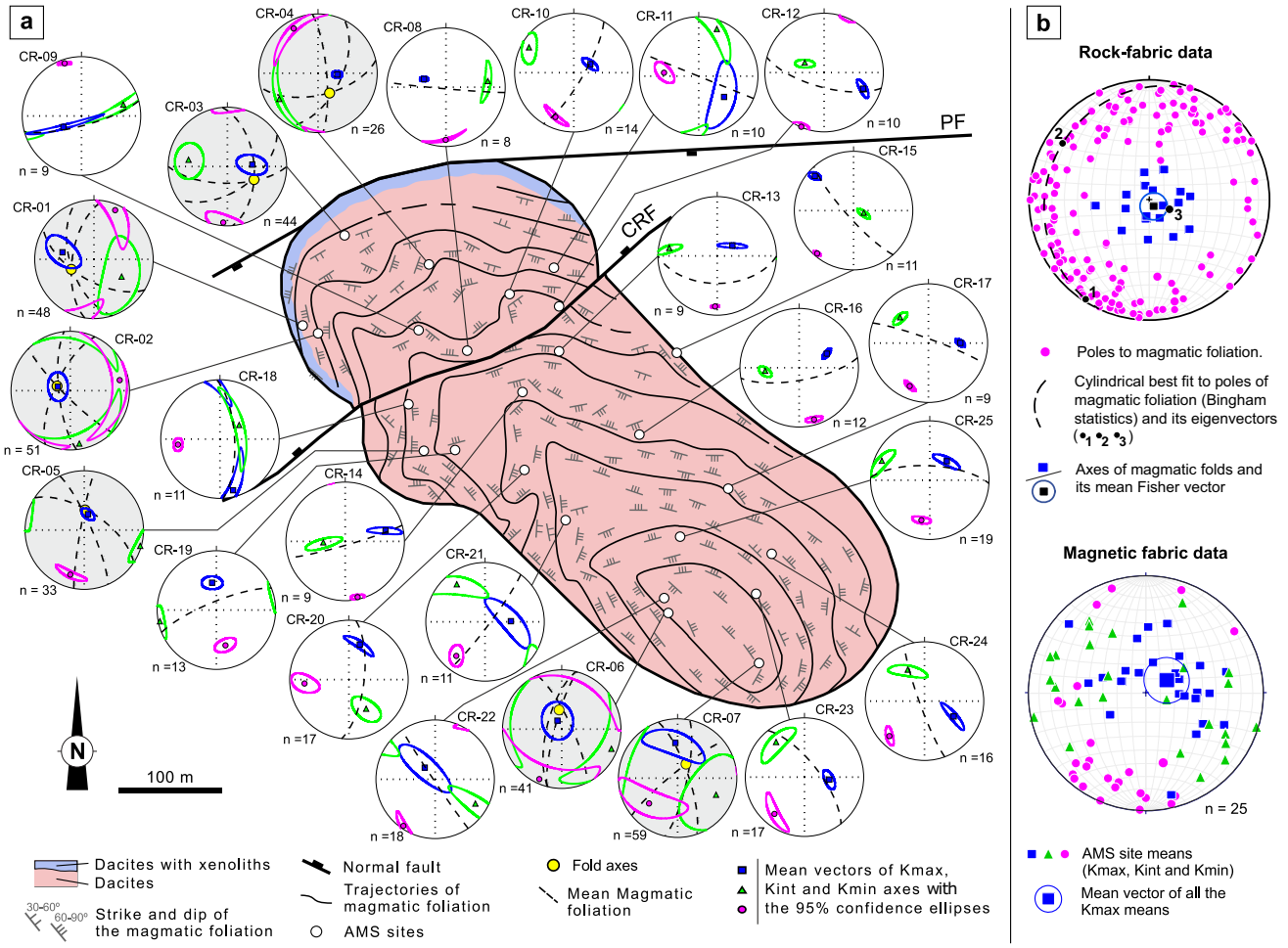

Fig. 9 **a** Trajectory map of the magmatic foliation. Stereoplots show mean AMS axes (Kmax, Kint and Kmin) with Jelinek confidence ellipses and mean magmatic foliation orientations at each site (data shown in Table 2). Gray stereoplots correspond to sites with meter-scale fold data. Pf: Pardos fault, CRF: Cerro Redondo fault. **b** Synthetic stereoplots summarizing structural and AMS data (see text for discussion)

through a relatively homogeneous body (Pinotti et al., 2010 and references therein). In the case of Cerro Redondo, the dacitic intrusion exhibits folds with irregular geometries, including frequent "C" interference patterns of Type 3 folds (Benn, 2005; D´Eramo et al., 2006; Manninen et al., 2008; Miller & Paterson, 1995; Pitcher & Berger, 1972) (Fig. 6e).

A key issue in the interpretation of such structures concerns the timing of fold development relative to the complete crystallization of the magma. In the present study, the presence of solid-state deformation features at folded sites (e.g. kinked biotites, Fig. 4) along with the overprinting of earlier magnetic fabrics by magmatic folds, supports the interpretation of passive folding affecting a pre-existing foliation prior to complete solidification of the magma.

To constrain the timing of fold development relative to the primary magmatic fabric, AMS data from folded sites were compared in both "in situ" and foliation coordinate systems (Fig. 11, Online Resource 1). The foliation coordinate system is constructed by rotating the AMS data of each sample so that the foliation plane is brought to a horizontal position. The Fold Test was not applied here, as the goal was not to determine the orientation of the magnetic data relative to a reference frame, but to evaluate whether the clustering or dispersion of the magnetic axes (Kmax or Kmin) occurred before or after folding. Moreover, unlike tectonic folds, magmatic folds develop synchronously with the acquisition of axial plunge.

AMS fabrics from folded sites in the "in situ" coordinate system typically shows a Kmax axes parallel or close to the fold axes, while Kmin axes are generally perpendicular to the magmatic foliation at the site scale. At foliation coordinates, AMS fabrics show the same magnetic fabric types as those found in unfolded sites at the outcrop scale (Fig. 11).

This comparison, using confidence angles from the Jelinek statistics, reveals an increase in the K_{12} and K_{23} angles (Fig. 12a), with a consistent Kmin (K_{31}) distribution.

Table 2 Directional results from AMS analysis for the studied sites: trend, plunge and angles of the confidence ellipses (Jelinek statistics) for Kmax, Kint and Kmin

Name	Kmax				Kint				Kmin			
	Trend	Plunge	K_{12}	K_{13}	Trend	Plunge	K_{21}	K_{23}	Trend	Plunge	K_{31}	K_{32}
CR-01	280	49	34	16	116	40	48	27	19	8	46	10
CR-02	296	71	15	8	147	16	55	14	55	9	55	9
CR-03	91	67	14	7	274	24	18	9	183	1	18	11
CR-04	94	63	7	5	235	22	50	5	331	15	50	6
CR-05	13	68	11	6	107	2	19	10	197	22	20	5
CR-06	341	75	22	13	130	13	73	18	222	8	73	15
CR-07	2	43	35	14	117	25	55	34	228	37	55	16
CR-08	290	58	6	3	83	30	26	5	180	12	26	2
CR-09	239	61	58	3	76	28	58	4	342	7	8	3
CR-10	67	65	14	4	293	18	15	10	198	17	11	44
CR-11	129	44	47	17	22	18	47	10	276	41	18	9
CR-12	112	29	15	4	295	61	14	5	203	1	8	6
CR-13	56	65	21	3	278	19	21	4	183	16	5	2
CR-14	75	30	27	4	265	60	27	6	167	4	7	5
CR-15	312	13	11	4	107	75	11	3	220	6	4	3
CR-16	63	47	10	3	263	42	10	5	164	10	9	5
CR-17	90	45	8	4	311	37	11	6	204	22	9	3
CR-18	166	12	61	7	56	58	61	7	263	29	8	7
CR-19	351	51	14	10	258	3	17	9	166	39	14	10
CR-20	17	38	22	5	150	41	25	12	265	26	23	10
CR-21	89	54	45	13	322	23	45	12	220	26	17	9
CR-22	318	69	49	14	122	21	49	9	214	5	19	4
CR-23	96	55	14	6	320	26	28	12	219	21	28	7
CR-24	118	44	26	4	331	41	27	3	225	17	13	5
CR-25	42	55	20	6	291	14	21	8	192	32	12	5

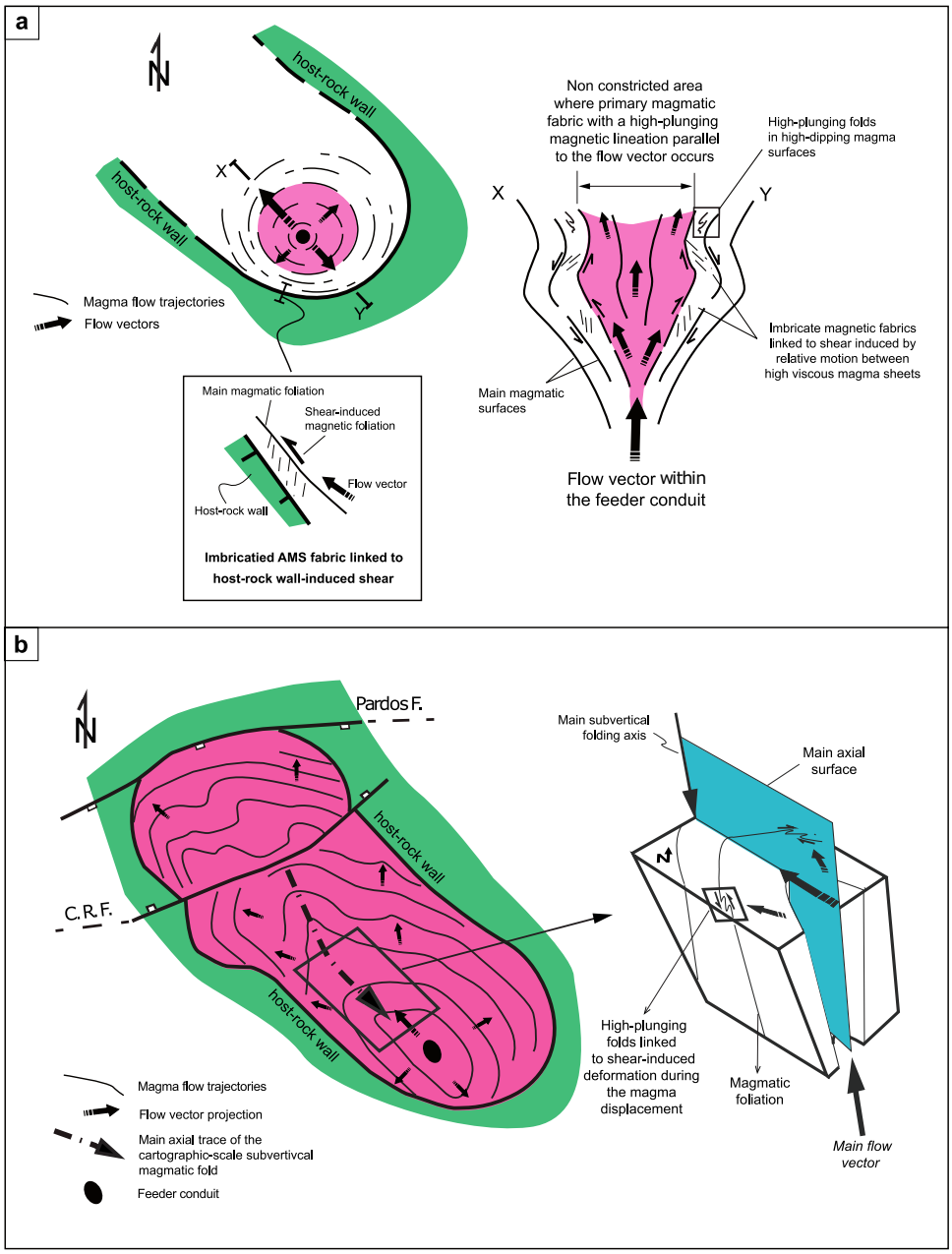

Fig. 10 **a** Kinematic interpretation during the emplacement of the early magmatic fabric. **b** Geometric and kinematic aspects related to magmatic folding

Using the "k" factor from the Fisher statistics (Fisher, 1953), Kmax data exhibit tighter clustering in "in situ" coordinates, with "k" values reaching up to 50, compared to values typically below 2 in foliation coordinates (Fig. 12b). Conversely, Kmin axes show improved clustering in foliation coordinates (Fig. 12b). These patterns indicate that the primary planar magnetic fabric pre-dates the folding process. This suggests that the magnetic fabric at folded sites corresponds to a well developed linear-planar fabric, where magnetic lineations are contained within the foliation surfaces.

Regionally, the distribution of asymmetrical magmatic folds, characterized by steep axial plunges parallel to magnetic lineation, Type 2/3 geometries and/or interference patterns of Type-3 folds (Ramsay, 1967), is compatible with shear deformation linked to viscous magma flow from the feeder zone and its progressive expansion toward the northwestern sector of the intrusion (Fig. 10b). The superposition of this deformation on a pre-existing planar fabric supports a progressive acquisition of a magnetic lineation (and the increase in anisotropy of the confidence ellipses and the decrease in anisotropy of the magnetic ellipsoid): initially forming within the magnetic foliation, then gradually aligning with the fold axis, and therefore with the elongation/amplification direction within the magmatic system. Thus, the variable orientation between magnetic foliation and the axes within the Jelinek ellipses reflects a continuous

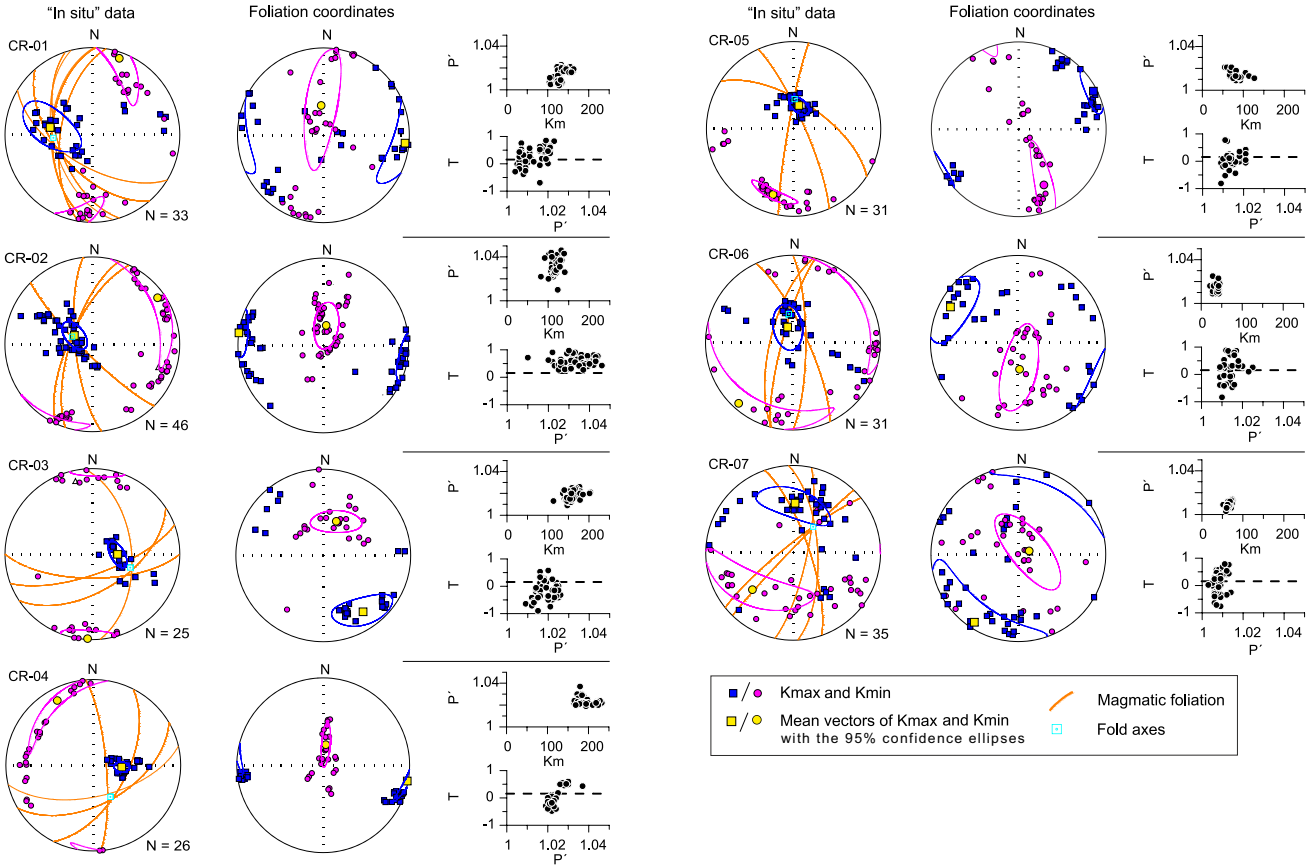

Fig. 11 Stereographic projection of AMS data in "in situ" and foliation coordinates, and plots of mean magnetic susceptibility (Km) vs. corrected degree of anisotropy (P'), and P' vs. shape parameter (T), for sites affected by meter-scale folding

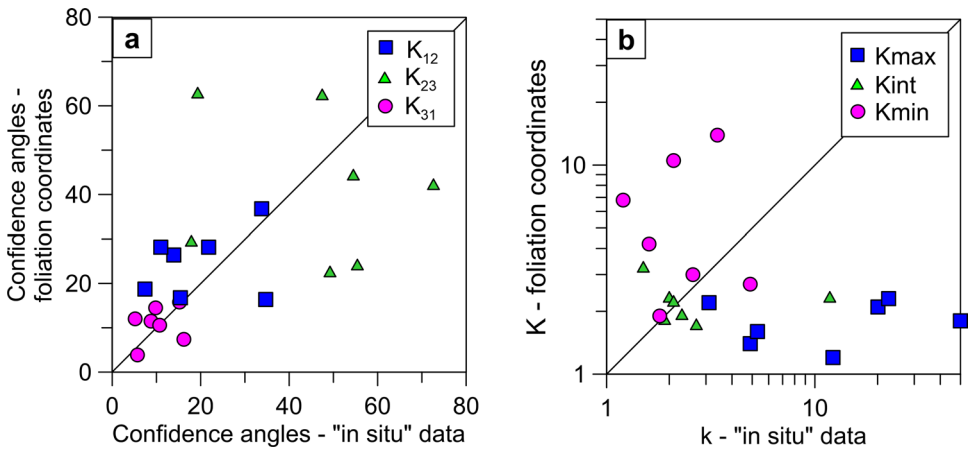

Fig. 12 **a** Comparison between the concentration (Jelinek confidence ellipses) of Kmax, Kint and Kmin orientations between "in situ" and foliation coordinates at AMS sites affected by magmatic folding. **b** Equivalent comparison using Fisher confidence cones

overprinting of the magmatic rock fabric due to the combined effects of magma pressure and subsequent folding.

Finally, the viscosity of the magma is the most decisive rheological factor in the acquisition of magmatic fabrics. Once crystal content exceeds ~ 30%, the magma behaves as a Binghamian fluid and the rock fabric results from the passive rotation of crystals (Fernández & Gasquet, 1994; Hrouda et al., 1999). Based on the calculations by McBirney (1993) using the data from Majarena et al. (2017a) and assuming a wet magma, the estimated viscosity of the Cerro Redondo magma ranges between 2.5×10^7 and 1.5×10^8 poise (Fig. 13). This supports the interpretation of the magmatic fabric as the result of the passive, crystal-scale rotational processes during flow.

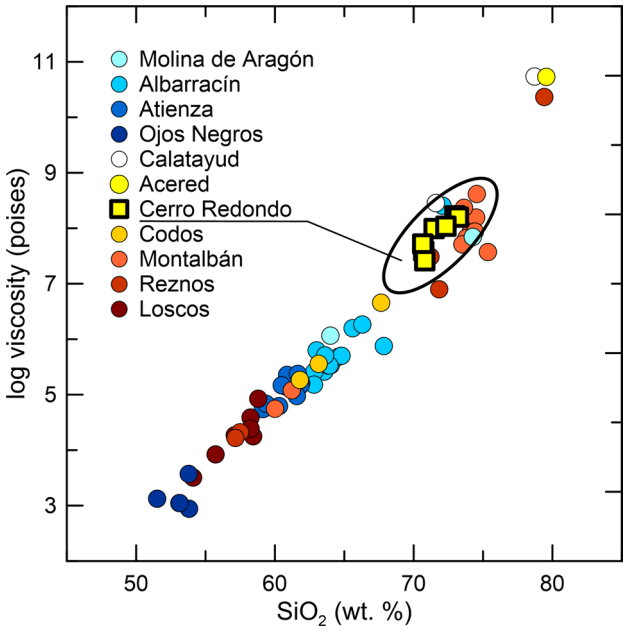

Fig. 13 Calculated melt viscosity versus SiO_2 content for representative outcrops of calc-alkaline magmatism in the Iberian Chain. Viscosity values are log_{10} of the melt viscosity (in Poise), assuming a wet magma conditions (calculations from McBirney, 1993). Geochemical compositions from Majarena et al. (2023b) and references therein

6.3 Geometry of the Cerro Redondo intrusion and emplacement sequence

As shown in the map view of magmatic foliation trajectories (Fig. 3), a sub-vertical magmatic feeder conduit is interpreted in the southeastern sector of the intrusion, where a concentric pattern of foliation trajectories is evident. This interpretation is further supported by the predominance of steeply dipping magmatic foliations, high-plunge magmatic fold axes and steeply plunging magnetic lineations in this sector (see sites CR-06, CR-22, CR-23 and CR-25).

Despite the overall parallelism between the northeastern and southwestern margins of the intrusion and the host rocks, the cross-cutting relationships at its northwestern and southeastern edges of the body indicate that the intrusion locally transects the host rocks. At the map scale, a NW–SE striking axial surface is defined by the curved magma flow trajectories (Fig. 3), suggesting a structural control during emplacement.

Tectonically, both local and regional evidence supports a connection between magma ascent/emplacement and the Pardos Fault, a major E–W trending late-Variscan strike-slip tensional fault associated with the emplacement of several early Permian intrusions (Majarena et al., 2017b; Fig. 1b). Additionally, the concentration of Variscan black shale xenoliths near the northwestern margin of the intrusion may indicate a buttressing effect of the fault against the direction of magma flow.

Our multidisciplinary study reveals that the emplacement and evolution of the Cerro Redondo intrusion occurred through two successive petro-structural stages (Fig. 14):

Initial stage. The first phase involved the injection of multiple pulses of less evolved magma, characterized by a low content of sanidine phenocrysts (6–13%), higher density and frequent host-rock xenoliths, through a sub-vertical feeder conduit. During this stage, a sub-vertical magmatic lineation developed. The presence of map-scale normal faults in the region suggests that pre-existing fractures played an active role in magma ascent (Fig. 14a). This stage likely occurred under a non-constricted, extensional tectonic regime (Fig. 10a).

Final stage. As the intrusion grew, progressively more evolved magma, with a higher content of sanidine phenocrysts (14–23%), lower density and without xenoliths, was emplaced. This more evolved magma underwent flattening, shearing and folding as it migrated toward the northwestern sector of the intrusion (Fig. 10b).

Cross-cutting relationships with the host rocks and the concentric magmatic foliation trajectories in the southeastern part of the intrusion, along with steep magmatic foliations, suggest that Cerro Redondo formed as a 3D, sub-vertical, asymmetrical dyke-like body elongated along a NW–SE direction (Fig. 14b). This interpretation is reinforced by the alignement between the intrusion's long axis and the main NW–SE trending axial surface that defines the magma flow architecture. We propose that magma propagation and growth toward the NW were facilitated by: (i) the presence of ductile, Lower Ordovician host-rocks, and (ii) sinistral flexural-slip motion parallel to the host-rock bedding planes, consistent with a strike-slip movement of the Pardos fault in a late-Variscan trans-tensional context (Fig. 14b).

As the intrusion expanded, magma progressively migrated northwestward, in parallel with the regional extension direction (Fig. 14b). In this model, the less evolved magma pulses were displaced toward the NW, while the more evolved (felsic) ones are accumulated near the feeder conduit. This petro-structural evolution is supported by the spatial variation in Km values, sample-density and the phenocrysts content sanidine and biotite (Figs. 6 and 14b), along with the NW-focused distribution of xenoliths.

The inferred tectonic setting for the Cerro Redondo emplacement aligns with reconstructions of the Late-Variscan geodynamic framework for the Iberian Chain (Capote, 1983; López-Gómez et al., 2002).

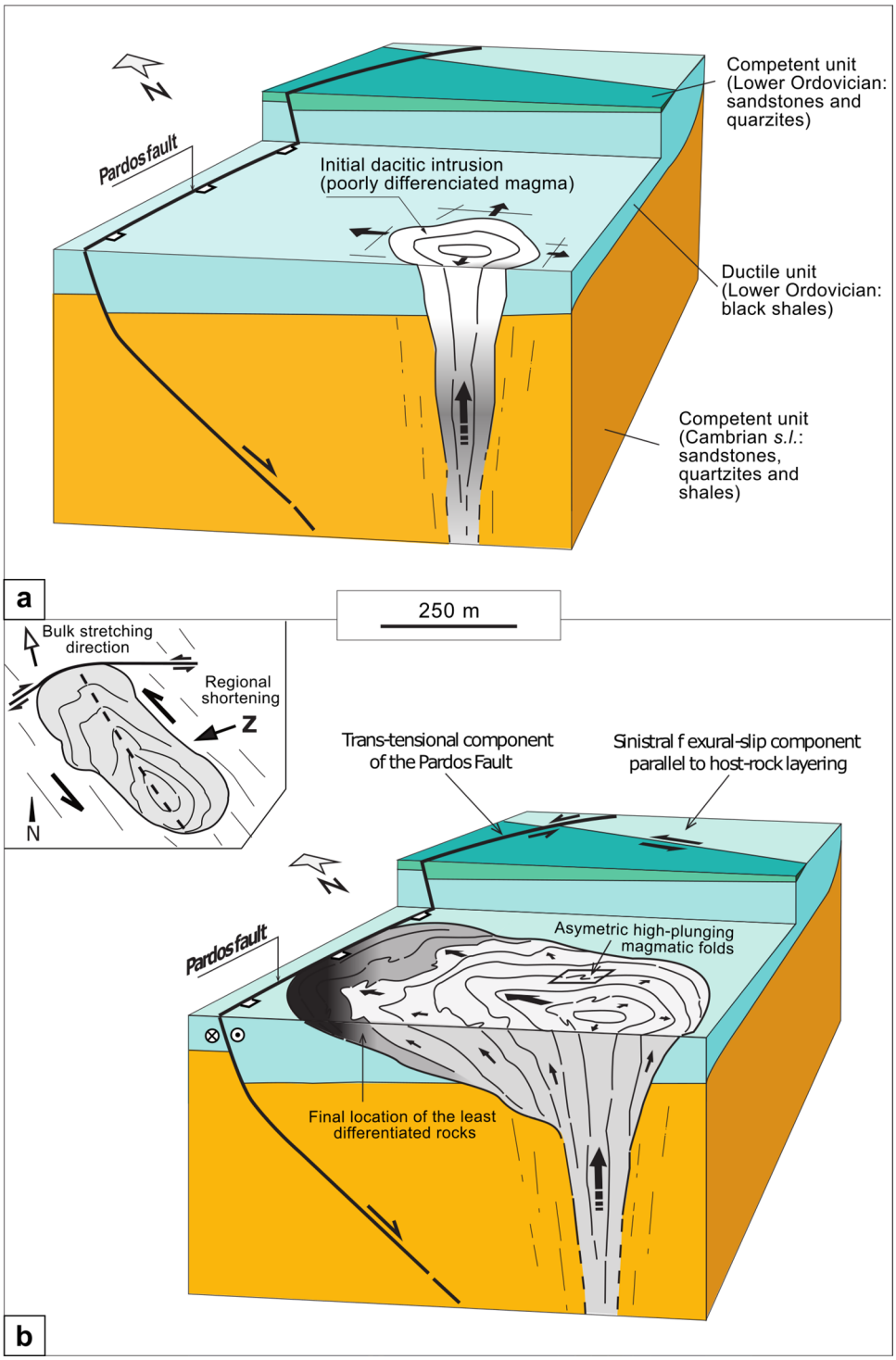

Fig. 14 Proposed emplacement and growth model of the Cerro Redondo intrusion before Alpine tilting. **a** Initial stage under a pure extensional tectonic regime. **b** Final stage: lateral expansion within a ductile Variscan unit, favored by a late-Variscan transtensional setting. Arrows indicate magma flow directions. The graphic scale corresponds to the frontal section. Inset: sinistral transtensional regime compatible with the development of the main NW–SE map-scale fold (bold dashed line) observed in the intrusion

7 Conclusions

The AMS and structural analysis of the Cerro Redondo dacitic intrusion (Iberian Chain, NE Spain) reveals an asymmetric igneous body with a sub-vertical feeder conduit and a main NW–SE-oriented elongation.

The observed parallelism between magmatic and magnetic foliations, as well as between magmatic fold axes and magnetic lineations, supports a strong correlation between magnetic and rock fabrics, confirming the normal character of the magnetic fabric. Low-field bulk susceptibility, sample density values and petrographic observations indicate a paramagnetic behaviour with AMS governed by biotite.

A subtle but significant zonation is identified, attributed to varying crystallization rates, with more felsic samples concentrated vertically above the interpreted intrusion feeder conduit, defined by a concentric magmatic foliation pattern.

The magnetic fabric displays a well-developed foliation, consistently aligned with the magmatic foliation throughout the intrusion. Magnetic lineations tend to lie within the magmatic foliation plane or align with sub-vertical fold axes at sites affected by metric- to decametric-scale magmatic folding. This parallelism is interpreted as reflecting the elongation or amplification direction during magma emplacement.

The integration of structural, petrographic and AMS data reveals three main petrostructural processes that controlled the emplacement and growth of the Cerro Redondo intrusion: (i) early formation of a planar-type magmatic fabric within the central sector of the feeder zone under a non-constrictive stress regime, (ii) shear-induced deformation of the earlier magmatic surfaces during successive emplacement pulses of viscous magma; and (iii) late-stage folding in the subsolidus state, prior to complete crystallization, affecting the primary planar magmatic fabric. Shear deformation processes likely operated throughout the emplacement history until full solidification.

The emplacement of the Cerro Redondo intrusion is interpreted to result from the activity of the Pardos Fault, under two successive late-Variscan extensional and strike-slip tectonic regimes. This study demonstrates that the combined application of magnetic fabric analysis and structural geology provides an effective approach for reconstructing the 3D emplacement history of subvolcanic igneous bodies.

Supplementary Information The online version contains supplementary material available at https://doi.org/10.1007/s41513-025-00327-4.

Acknowledgements This project was financed by the Aragón government, the research groups of Geotransfer-IUCA (E32_23R) and Aragosaurus (E18_20R), the Spanish government (RTI2018-093419-B-I00 and PID2019-108753GB-C22), the ERDF program (2014-2020) and the subsidies destined to the hiring of predoctoral researchers for the period 2017-2021, co-financed with the Operational Program FSE Aragón 2014-2020. We would like to thank the Magnetometry Unit of the CACTI (University of Vigo) for the measurements of the hysteresis cycles and the *Servicio General de Apoyo a la Investigación* (SAI) of the University of Zaragoza for its help in obtaining the rest of the measurements used in this article. This work greatly benefited from the constructive and insightful comments provided by the editor, David Orejana, as well as by Emilio Pueyo and another anonymous reviewer.

Funding Open Access funding provided thanks to the CRUE-CSIC agreement with Springer Nature. The research leading to these results received funding from the Aragón Government (Operational Program FSE Aragón 2014-2020; Geotransfer-IUCA research group: E32_23R and project ERDF 2014-20 OP) and the Ministry of Science and Innovation of the Government of Spain (project PID2019-108753GB-C22).

Declarations

Conflict of interest On behalf of all authors, the corresponding author states that there is no conflict of interest.

References

Aranguren, A., Tubia, J., Bouchez, J. L., & Vigneresse, J. L. (1996). The Guitiriz granite, Variscan belt of northern Spain: Extension-controlled emplacement of magma during tectonic escape. *Earth and Planetary Science Letters, 139*(1–2), 165–176. https://doi.org/10.1016/0012-821X(95)00239-9

Balsley, J. R., & Buddington, A. F. (1960). Magnetic susceptibility anisotropy and fabric of some Adirondack granites and orthogneisses. *American Journal of Science, 258*(6), Article e20.

Benn, K. (2005). Late Archaean Kenogamissi complex, Abitibi Subprovince, Ontario, Canada: doming, folding and deformation-assisted melt remobilisation during syntectonic batholith emplacement. In S. Ishihara, W. E. Stephens, S. L. Harley, M. Arima, & T. Nakajima (Eds.), *The Origin of Granites and Related Rocks. Fifth Hutton Symposium* (pp. 297–307). The Geological Society of America. https://doi.org/10.1130/0-8137-2389-2.297

Bouchez, J. L., Gleizes, G., Djouadi, T., & Rochette, P. (1990). Microstructure and magnetic susceptibility applied to emplacement kinematics of granites: The example of the foix pluton (French pyrenees). *Tectonophysics, 184*, 157–171.

Bouchez, J. L., Delas, C., Gleizes, G., Nedelec, A., & Cuney, M. (1992). Submagmatic microfractures in granites. *Geology, 20*, 35–38. https://doi.org/10.1130/0091-7613(1992)020%3c0035:SMIG%3e2.3.CO;2

Bouchez, J. L. (1997). Granite is Never Isotropic: An Introduction to AMS Studies of Granitic Rocks. In J. L. Bouchez, D. H. W. Hutton, & W. E. Stephens (Eds.), *Granite: From Segregation of Melt to Emplacement Fabrics. Petrology and Structural Geology* (pp. 95–112). Kluwer.

Buttner, H. L. (1999). The geometric evolution of structures in granite during continous deformation from magmatic to solid-state conditions: An example from the central European Variscan Belt. *American Mineralogist, 84*, 1781–1792. https://doi.org/10.2138/am-1999-11-1207

Calvín-Ballester, P., Casas-Sainz, A. M., & Villalaín, J. J. (2012). Sobre el origen de una anomalía magnética inversa en el norte de la Cordillera Ibérica (Unidad de Herrera, Rama Aragonesa). *Geotemas, 13*, 1128–1131.

Calvín, P., Casas, A. M., Villalaín, J. J., & Tierz, P. (2014). Reverse magnetic anomaly controlled by Permian Igneous rocks in the Iberian Chain (N Spain). *Geologica Acta, 12*(3), 0193–0207. https://doi.org/10.1344/GeologicaActa2014.12.3.2

Capote, R. (1983). La fracturación subsecuente a la origenia hercínica. In J. A. Comba (Ed.), *Libro Jubilar J. M. Ríos* (pp. 17–25). IGME.

Carls, P. (1983). La Zona Asturoccidental-leonesa en Aragón y el macizo del Ebro como prolongación del Macizo Cantábrico. In J. A. Comba (Ed.), *Libro Jubilar J.M. Ríos* (Vol. 3, pp. 11–32). IGME.

Clarke, D. B., & Clarke, G. K. C. (1998). Layered granodiorites at Chebucto Head, South Mountain batholith, Nova Scotia. *Journal of Structural Geology, 20*(9–10), 1305–1324. https://doi.org/10.1016/S0191-8141(98)00067-4

Chadima, M., & Hrouda, F. (2009). *Cureval 8.0: Thermomagnetic curve browser for windows*. Agico Inc.

Chadima, M., & Jelinek, V. (2008). Anisoft 4.2. Anisotropy data browser. *Contributions to Geophysics and Geodesy, 38*(Spec. Issue), 38–41.

D´Eramo, F. J., Vegas, N., Pinotti, L. P., Tubía, J. M., & Coniglio, J. E. (2006). Pliegues magmaticos en el pluton trondhjemítico de La Fronda, Sierras Pampeanas de Córdoba, Argentina. *Geogaceta, 39*, 15–18.

Fazio, E., Patrizia, F., Damiano, R., & Rosolino, C. (2020). Submagmatic to solid-state deformation microstructures recorded in cooling granitoids during exhumation of Late-Variscan crust in north-eastern Sicily. *Geosciences*. https://doi.org/10.3390/geosciences10080311

Ferndez, A. N., & Gasquet, D. R. (1994). Relative rheological evolution of chemical contrasted coeval magmas: example of the Tichka plutonic complex (Morocco). *Contribution in Mineralogy and Petrology, 116*, 316–326. https://doi.org/10.1007/BF00306500

Gawęda, A., & Szopa, K. (2012). The origin of magmatic layering in the High Tatra granite, Central Western Carpathians–implications for the formation of granitoid plutons. *Earth and Environmental Science Transactions of the Royal Society of Edinburgh, 102*(2), 129–144. https://doi.org/10.1017/S1755691012010146

geoFisher, R. A. (1953). Dispersion on a sphere. *Proceedings of the Royal Society of London Series A Mathematical and Physical Sciences, 217*(1130), 295–305.

Gil-Imaz, A., Pocovi, A., Lago, M., Gale, C., Arranz, E., Rillo, C., & Guerrero, E. (2006). Magma flow and thermal contraction fabric in tabular intrusions inferred from AMS analysis. A case study in a late-Variscan folded sill of the Albarracín Massif (southeastern Iberian Chain, Spain). *Journal of Structural Geology, 28*(4), 641–653. https://doi.org/10.1016/j.jsg.2005.12.016

Gil Imaz, A., Lago San José, M., Pueyo Anchuela, Ó., & Galé, C. (2009). Fábrica magnética (ASM) de diques andesíticos autunienses con enclaves corticales del sector de Maicas (Anticlinal de Montalbán, Cadena Ibérica Oriental). *Geogaceta, 46*, 31–34.

Gleizes, G., Nedelec, A., Bouchez, J.-L., Autran, A., & Rochette, P. (1993). Magnetic susceptibility of the Mont Louis – Andorra ilmenite-type granite (Pyrenees): a new tool for the petrographic characterization and regional mapping of zoned granite plutons. *Journal of Geophysical Research, 98*, 4317–4331. https://doi.org/10.1029/92JB01590

Guillet, P., Bouchez, J. L., & Wagner, J. J. (1983). Anisotropy of magnetic susceptibility and magmatic structures in the Guérande granite massif (France). *Tectonics, 2*(5), 419–429. https://doi.org/10.1029/TC002i005p00419

Henkel, H. (1976). Studies of density and magnetic properties of rocks from Northern Sweden. *Pure and Applied Geophysics, 114*, 235–249.

Hrouda, F., Taborska, S., Schulmann, K., Jezek, J., & Dolejs, D. (1999). Magnetic fabric and rheology of co-mingled magmas in the Nasavrky Plutonic Complex (E Bohemia): implications for intrusive strain regime and emplacement mechanism. *Tectonophysics, 307*, 93–111. https://doi.org/10.1016/S0040-1951(99)00121-3

Hrouda, F. (1982). Magnetic anisotropy and its application in geology and geophysics. *Geophysical Surveys, 5*, 37–82.

Hrouda, F. (1994). A technique for the measurement of thermal changes of magnetic susceptibility of weakly magnetic rocks by the CS-2 apparatus and KLY-2 kappabridge. *Geophysical Journal International, 118*, 604–612.

Hutton, D. H. (1988). Granite emplacement mechanisms and tectonic controls: Inferences from deformation studies. *Earth and Environmental Science Transactions of the Royal Society of Edinburgh, 79*(2–3), 245–255. https://doi.org/10.1017/S0263593300014255

Jackson, M., Gruber, W., Marvin, J., & Banerjee, S. K. (1988). Partial anhysteretic remanence and its anisotropy: Applications and grainsize-dependence. *Geophysical Research Letters, 15*(5), 440–443. https://doi.org/10.1029/GL015i005p00440

Jelinek, V. (1977). *The statistical theory of measuring anisotropy of magnetic susceptibility of rocks and its application*. Geofyzika.

Jelinek, V. (1981). Characterization of the magnetic fabric of rocks. *Tectonophysics, 79*, 63–67. https://doi.org/10.1016/0040-1951(81)90110-4

Jordanova, D., & Jordanova, N. (2016). Thermomagnetic behavior of magnetic susceptibility-heating rate and sample size effects. *Frontiers in Earth Science, 3*, Article 90. https://doi.org/10.3389/feart.2015.00090

Jousselin, D., Morales, L. F., Nicolle, M., & Stephant, A. (2012). Gabbro layering induced by simple shear in the Oman ophiolite Moho transition zone. *Earth and Planetary Science Letters, 331*, 55–66. https://doi.org/10.1016/j.epsl.2012.02.022

Lago, M., Alvaro, J., Arranz, E., Pocoví, A., & Vaquer, R. (1992). Condiciones de Emplazamiento, Petrología y Geoquímica de las riolitas, calco-alcalinas y stephaniense-pérmicas, en las cadenas ibéricas. *Cuadernos Del Laboratorio Xeolóxico De Laxe, 17*, 187–198.

Lago, M., Arranz, E., Pocoví, A., Galé, C., & Gil-Imaz, A. (2004). Lower Permian magmatism of the Iberian Chain, Central Spain, and its relationship to extensional tectonics. *Geological Society London Special Publication, 223*, 465–490. https://doi.org/10.1144/GSL.SP.2004.223.01.20

Lago, M., Gil, A., Arranz, E., Galé, C., & Pocoví, A. (2005). Magmatism in the intracratonic Central Iberian basins during the Permian: Paleoenvironmental consequences. *Palaeogeography, Palaeoclimatology, Palaeoecology, 229*, 83–103. https://doi.org/10.1016/j.palaeo.2005.06.032

López-Gómez, J., Arche, A., & Pérez-López, A. (2002). Permian and Triassic. In W. Gibbons & T. Moreno (Eds.), *The Geology of Spain.* Geological Society London.

Majarena, U., Lago, M., Galé, C., Esteban, J. J., & García de Madinabieitia, S. (2017a). El magmatismo Pérmico Inferior de la Sierra de Pardos (Rama Aragonesa de la Cordillera Ibérica, Zaragoza): Petrología y geoquímica. *Geogaceta, 61*, 111–114.

Majarena, U., Gil, A., Lago, M., & Galé, C. (2017b). La intrusion de Cerro Redondo (Pérmico inferior, Cordillera Ibérica, Zaragoza): Reconstrucción 3D y modelo de emplazamiento. *Geogaceta, 61*, 119–122.

Majarena, U., Esteban, J. J., Galé, C., Gil-Imaz, A., & Lago, M. (2023a). Cisuralian calc-alkaline magmatism in the Herrera Unit of the Iberian Chain (Cantabrian Zone of the Iberian Massif, Spain): age and geodynamic constrains from U-Pb laser ablation inductively coupled plasma mass spectrometry zircon analysis. *Journal of the Geological Society, 180*, 6843778. https://doi.org/10.1144/jgs2022-102

Majarena, U., Galé, C., Esteban, J. J., Lago, M., & Gil-Imaz, A. (2023b). The magmatism of Atienza (NW Iberian Chain, Spain): Age origin and architecture of the magmatic plumbing system. *Journal of Iberian Geology, 49*(1), 47–69. https://doi.org/10.1007/s41513-023-00206-w

Manninen, T., Eerola, T., Mäkitie, H., Vuori, S., Luttinen, A., Sénvano, A., & Manhiça, V. (2008). The Karoo volcanic rocks and related intrusions in southern and central Mozambique. *Geological Survey of Finland, Special Paper, 48*, 211–250.

McBirney, A. R. (1993). *Igneous petrology*. Jones & Bartlett Learning.

Megerssa, L., Verner, K., Buriánek, D., & Sláma, J. (2020). Emplacement and thermal effect of post-collisional Chewo Pluton (Arabian-Nubian Shield); Implication for late East-African Orogeny. *Journal of African Earth Sciences, 162*, Article 103685. https://doi.org/10.1016/j.jafrearsci.2019.103695

Miller, R.B., & Paterson, S.R. (1995). Pluton emplacement in arcs: a crustal-scale recycling process. In M. Brown & M. Piccoli, (Eds.), *The Origen of Granites and Related Rocks. Third Hutton Symposium Abstracts.* U.S. Geological Survey Circular 1129 (pp. 111–112).

Namur, O., Abily, B., Boudreau, A. E., Blanchette, F., Bush, J. W. M., Ceuleneer, G., Charlier, B., Donaldson, C. H., Duchesne, J. C., Higgins, M. D., Morata, D., Nielsen, T. F. D., Oriscoll, D., Pang, K. N., Peacock, T., Spandler, C. J., Toramaru, A., & Veksler, I. V. (2015). Igneous Layering in Basaltic Magma Chambers. In B. Charlier, O. Namur, R. Latypov, & C. Tegner (Eds.), *Layered Intrusions* (pp. 75–152). Springer. https://doi.org/10.1007/978-94-017-9652-1

Passchier, C. W., & Trouw, R. A. J. (2005). Microtectonics. *Springer*. https://doi.org/10.1007/3-540-29359-0

Paterson, S. R., Fowler, T. K., Jr., Schmidt, K. L., Yoshinobu, A. S., Yuan, E. S., & Miller, R. B. (1998). Interpreting magmatic fabric patterns in plutons. *Lithos, 44*(1–2), 53–82. https://doi.org/10.1016/S0024-4937(98)00022-X

Paterson, S. R., & Vernon, R. H. (1995). Bursting the bubble of ballooning plutons: A return to nested diapirs emplaced by multiple processes. *Geological Society of America Bulletin, 107*(11), 1356–1380. https://doi.org/10.1130/0016-7606(1995)107%3c1356:BTBOBP%3e2.3.CO;2

Paterson, S. R., Vernon, R. H., & Tobisch, O. T. (1989). A review of criteria for the identification of magmatic and tectonic foliations in granitoids. *Journal of Structural Geology, 11*(3), 349–363. https://doi.org/10.1016/0191-8141(89)90074-6

Pawley, M. J., & Collins, W. J. (2002). The development of contrasting structures during the cooling and crystallisation of a syn-kinematic pluton. *Journal of Structural Geology, 24*, 469–483. https://doi.org/10.1016/S0191-8141(01)00069-4

Pinotti, L. P., D´Eramo, F. J., Demartis, M., Coniglio, J. E., & Tubía-Martínez, J. M. (2010). Estructuras magmàticas en granitos. *Revista De La Asociacion Geologica Argentina, 67*(4), 562–572.

Pinotti, L., Tubía, J. M., D'Eramo, F., Vegas, N., Sato, A. M., Coniglio, J., & Aranguren, A. (2006). Structural interplay between plutons during the construction of a batholith (Cerro Aspero batholith, Sierras de Córdoba, Argentina). *Journal of Structural Geology, 28*(5), 834–849. https://doi.org/10.1016/j.jsg.2006.02.004

Pinotti, L. P., D'Eramo, F. J., Weinberg, R. F., Demartis, M., Tubía, J. M., Coniglio, J. E., Radice, S., Maffini, M. N., & Aragón, E. (2016). Contrasting magmatic structures between small plutons and batholiths emplaced at shallow crustal level (Sierras de Córdoba, Argentina). *Journal of Structural Geology, 92*, 46–58. https://doi.org/10.1016/j.jsg.2016.09.009

Pitcher, W. S., & Berger, A. R. (1972). *The geology of Donegal: A study of granite emplacement and unroofting*. Wiley.

Pons, J., Barbey, P., Nachit, H., & Burg, J. P. (2006). Development of igneous layering during growth of pluton: The Tarçouate Laccolith (Morocco). *Tectonophysics, 413*, 271–286. https://doi.org/10.1016/j.tecto.2005.11.005

Porquet, M., Pueyo, E. L., Román-Berdiel, T., Olivier, P., Longares, L. A., Cuevas, J., Ramajo, J., the Geokin3DPyr working group. (2017). Anisotropy of magnetic susceptibility of the Pyrenean granites. *Journal of Maps, 13*(2), 438–448. https://doi.org/10.1080/17445647.2017.1302364

Pueyo-Anchuela, Ó., Casas-Sainz, A. M., Pueyo, E. L., Juan, A. P., & Imaz, A. G. (2013). Analysis of the ferromagnetic contribution to the susceptibility by low field and high field methods in sedimentary rocks of the Southern Pyrenees and Northern Ebro foreland basin (Spain). *Terra Nova, 25*(4), 307–314. https://doi.org/10.1111/ter.12037

Pueyo, E. L., Román-Berdiel, T., Calvín, P., Bouchez, J. L., Beamud, E., Ayala, C., & García-Lobón, J. L. (2022). Petrophysical characterization of non-magnetic granites; Density and magnetic susceptibility relationships. *Geosciences, 12*(6), Article 240. https://doi.org/10.3390/geosciences12060240

Ramsay, J. G. (1967). *Folding and fracturing of rocks*. Mc Graw Hill Book Company.

Rochette, P. (1987). Magnetic susceptibility of the rock matrix related to magnetic fabric studies. *Journal of Structural Geology, 9*(8), 1015–1020. https://doi.org/10.1016/0191-8141(87)90009-5

Román-Berdiel, T., Pueyo-Morer, E. L., & Casas-Sainz, A. M. (1995). Granite emplacement during contemporary shortening and normal faulting: Structural and magnetic study of the Veiga Massif (NW Spain). *Journal of Structural Geology, 17*(12), 1689–1706. https://doi.org/10.1016/0191-8141(95)00062-I

Sant'Ovaia, H., Cruz, C., Gonçalves, A., Nogueira, P., & Noronha, F. (2024). Deciphering Iberian Variscan Orogen Magmatism Using the Anisotropy of Magnetic Susceptibility from Granites. *Minerals, 14*, 309. https://doi.org/10.3390/min14030309

Stacey, F. D. (1960). Magnetic anisotropy of igneous rocks. *Journal of Geophysical Research, 65*(8), 2429–2442. https://doi.org/10.1029/JZ065i008p02429

Tarling, D. H., & Hrouda, F. (1993). *The magnetic anisotropy of rocks*. Springer.

Tauxe, L., Pick, T., & Mullender, T. A. T. (1996). Potbellies, wasp-waists, and superparamagnetism in magnetic hysteresis. *Journal of Geophysical Research: Solid Earth, 101*(B1), 571–583. https://doi.org/10.1029/95JB03041

Van der Voo, R., & Klootwijk, C. T. (1972). Paleomagnetic reconnaissance study of the Flamanville granite, with special reference to the anisotropy of its susceptibility. *Geologie En Mijnbouw, 51*(6), 609–617.

Wolf, R. (1980). The lower and upper boundary of the Ordovician System of selected regions (Celtiberia Eastern Sierra Nevada) in Spain. Part I: The lower Ordovician sequence of Celtiberia. *Neues Jahrbuch Für Geologie und Paläontologie Abhandlungen, 160*(1), 118–137. https://doi.org/10.1127/njgpa/160/1980/118